

Label-Free Single-Molecule Thermoscopy Using a Laser-Heated Nanopore

Hirohito Yamazaki,[†] Rui Hu,^{†,§} Robert Y. Henley,[†] Justin Halman,[‡] Kirill A. Afonin,[‡] Dapeng Yu,[§] Qing Zhao,[§] and Meni Wanunu^{*,†}

[†]Department of Physics, Northeastern University, Boston, Massachusetts 02115, United States

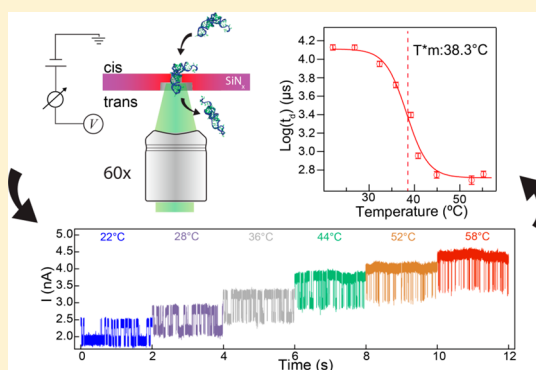
[‡]Department of Chemistry, University of North Carolina at Charlotte, 9201 University City Boulevard, Charlotte, North Carolina 28223, United States

[§]State Key Laboratory for Mesoscopic Physics, School of Physics, Peking University, Beijing 100871, People's Republic of China

S Supporting Information

ABSTRACT: When light is used to excite electronic transitions in a material, nonradiative energy during relaxation is often released in the form of heat. In this work, we show that photoexcitation of a silicon nitride nanopore using a focused visible laser results in efficient localized photothermal heating, which reduces the nearby electrolyte viscosity and increases the ionic conductance. In addition, a strong localized thermal gradient in the pore vicinity is produced, evidenced by finite-element simulations and experimental observation of both ion and DNA thermophoresis. After correcting for thermophoresis, the nanopore current can be used as a nanoscale thermometer, enabling rapid force thermoscopy. We utilize this to probe thermal melting transitions in synthetic and native biomolecules that are heated at the nanopore. Our results on single molecules are validated by correspondence to bulk measurements, which paves the way to various biophysical experiments that require rapid temperature and force control on individual molecules.

KEYWORDS: Nanopore, thermophoresis, optics, melting kinetics, single molecule



Interrogating the structural and dynamic properties of biomolecules has revealed a plethora of information about the roles various molecules play in life. While various tools for studying DNA, RNA, and proteins are available, recent advances in nanotechnology have enabled new devices that allow single molecule probing. Among these tools, the nanopore allows the electrical detection of the properties of individual unlabeled molecules at high throughput.^{1–4} Nanopores can probe entities as small as hydrogen isotopes⁵ to ones as large as viruses and cells,⁶ and everything in between. On the molecular level various features in macromolecules have been probed, including the stability of duplex DNA molecules,⁷ secondary structure in RNA molecules,^{8,9} and the sequence of DNA¹⁰ and RNA molecules.¹¹

The principle of nanopore sensing involves the application of a voltage across a membrane separating two chambers, each containing some electrolyte solution, through which a nanopore forms the solitary fluidic connection between the chambers. This produces a steady-state ion current across the pore, also resulting in a highly localized electric field in the pore. The field, which protrudes outside the pore confines, draws charged molecules into and through the nanopore. During this process, the ion flux is impeded, resulting in a

distinct electrical signature that represents the molecular occlusion of the pore.

Various experimental parameters can influence the signal in a nanopore-based study, including the pore geometry,¹² applied voltage (force),¹³ electrolyte ionic strength,¹⁴ and hydrostatic pressure.¹⁵ In addition to these, temperature is an important parameter that can affect molecular transport kinetics, molecular structure, and molecular stability. A common method to control temperature in a nanopore is to enclose the nanopore cell in a heating/cooling chamber.¹⁶ However, this method is often slow and subjects all of the molecules in the bath to the same temperature, regardless of whether they are interrogated in the nanopore or not. More elegant versions of experiments with temperature as a variable involve local and rapid heating of some interrogation volume that contains a molecule of interest. For example, FRET-based thermal studies on single DNA molecules have been reported recently, in which a pulsed IR beam was used to locally induce temperature changes and a coincident visible laser was used to probe FRET signal.¹⁷ Also, plasmonic enhancement of temperature has been

Received: August 31, 2017

Revised: October 3, 2017

Published: October 4, 2017

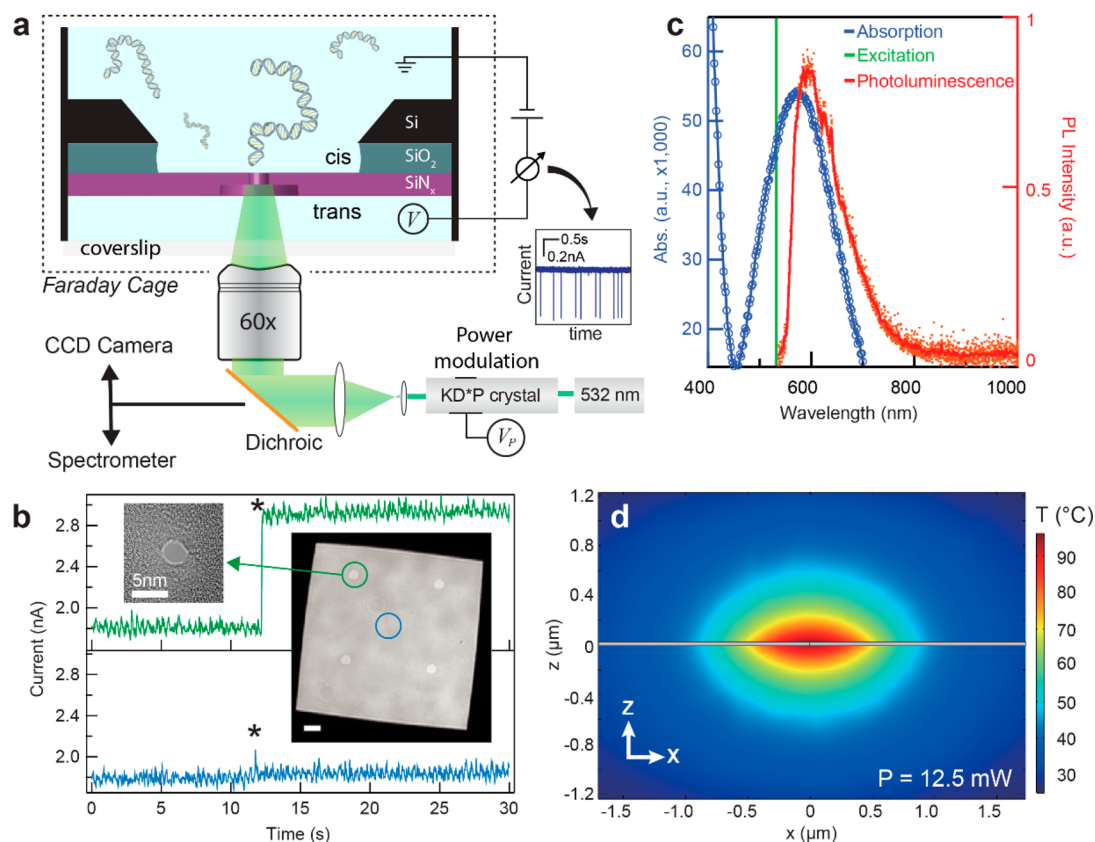


Figure 1. Laser-induced nanopore heating. (a) Schematic of our setup. Collimated 532 nm beam overfills the back plane of a 60 \times objective lens, which is used to focus the light on a SiN_x solid-state nanopore fabricated in a prethinned region. A pair of electrodes is used to apply bias and measure current across the nanopore. Molecular translocation induces transient blockades in the current signal (current vs time trace shows 500 bp DNA translocation events at $V = 300$ mV, pore diameter = 2.7 nm). The laser power is controlled using an electro-optic modulator (up to 800 \times attenuation, ~ 4 μ s response time). (b) Inset, right: Top-view of a back-illuminated 50 μ m \times 50 μ m freestanding 50-nm-thick SiN_x membrane with a pattern of four 25-nm-thick circular regions (scale bar = 5 μ m). A 3 nm diameter pore is drilled in one of the thin regions (green circle, left inset is a pore TEM image). Top and bottom current traces show the impact on the current ($V = 200$ mV) of a 10 mW laser, switched on at ~ 12 –13 s, either on nanopore (top, green circle) or off the nanopore (bottom, blue circle). (c) Absorbance spectrum of 200-nm-thick SiN_x membrane (blue, arrow points to axis) and photoluminescence spectrum (red, arrow points to axis) of 50-nm-thick freestanding SiN_x membrane excited by a 532 nm laser spot (green arrow at 532 nm). (d) Simulation of the steady-state temperature distribution, calculated using a 2D finite-element COMSOL simulation (see SI for details). A 42.5-nm-thick SiN_x membrane that has a nanopore through its center is surrounded by water, and nonradiative decay following a 12.5 mW laser excitation is incident on the membrane.

demonstrated to rapidly affect temperatures locally, being used, for example, for killing target cells.¹⁸

Recently, a protein nanopore was chemically conjugated to a plasmonic system that consists of several gold nanoparticles, and optical control over temperature around the nanopore was demonstrated by showing the enhanced ionic current through the pore.¹⁹ In this system, light absorption excites plasmonic oscillations in the gold nanoparticles, which heats the nearby electrolyte solution. This in turn reduces the electrolyte viscosity and increases ion mobility, measured as an increased ion-current through the pore. In another system, DNA melting using biological pore heated using an IR-based direct absorption heating of the aqueous medium was recently demonstrated,²⁰ with >100 ms required for thermal steady-state in this nonplasmonic configuration. A more sophisticated approach involves infrared laser irradiation of a plasmonic bowtie structure around the pore, which also allows temperature control.^{21–25}

In this report, we study in detail the interactions between a focused laser beam and a solid-state nanopore fabricated in a thin silicon nitride (SiN_x) membrane using electron beam irradiation. We find that photoexcitation of the pore using a

focused green laser beam induces electronic transitions in the membrane material. However, in contrast with an earlier report that associated this excitation with an increased surface charge near the pore,²⁶ we find here that excitation leads to localized heating of the nanopore surroundings via nonradiative relaxation pathways. This rapid nonradiative transition that leads to heating occurs at faster rates than measurable using our electronics (sub microsecond time scales), thereby allowing instant control over the nanopore temperature by electro-optic modulation of the laser power (P). We provide here a quantitative model that describes our heating results. Experimental evidence for our observations includes: (1) surface charge density is independent of P during laser irradiation, (2) evidence for ion and DNA thermophoresis, which affects the local concentration of each species near the pore, and (3) observation of thermal melting transitions in control three-way junction (3WJ) DNA molecules with known melting points. Finally, we study thermal melting of a tRNA (tRNA) molecule and show that melting can be detected as a transition to faster transit times that are also voltage dependent, as consistent with force-induced destabilization of the molecule.

Figure 1a displays a schematic diagram of our setup (not to scale, for more details see Supporting Information, SI, Figure S1). Our device is a Si chip that contains a noise-reducing SiO₂ layer below a free-standing SiN_x membrane that contains a nanopore through it. Prior to making a nanopore (3–5 nm diameter), a periodic array of thinned SiN_x circles (~2–3 μm diameter) is fabricated on each chip, to serve as an optical marker for pore localization. The chip is assembled in a fluidic cell with *cis* and *trans* chambers that contain an aqueous electrolyte. The bottom of the cell is a glass coverslip that allows optical interrogation using an inverted microscope. An electrode (Ag/AgCl) is placed in each reservoir, and the applied voltage leads to a steady-state current that is measured using a patch clamp amplifier. Further, when a sample of macromolecules is placed in the *cis* chamber and voltage is applied, the passage of these molecules through the pore is indicated by transient blockade events. In Figure 1b we highlight the impact of laser irradiation on the ion current through the pore: applying voltage ($V = 200$ mV) across the pore and switching on the laser, focused on the pore (green circle), from 0 to 10 mW (green trace, laser on at asterisk), results in an instantaneous enhancement of the ion current. In contrast, when the beam is focused on the membrane at a position that is ~15 μm away from the pore (blue circle), we find nearly no enhancement in the ion current (blue trace). This ionic current enhancement, documented in a recent study,²⁶ suggests that photoexcitability of the SiN_x is responsible for the observed effect. In Figure 1c, we show the absorbance spectrum of 200 nm thick SiN_x deposited on quartz (blue), as well as a photoluminescence (PL) spectrum of 50-nm-thick freestanding SiN_x under 532 nm laser excitation (red). From Figure 1c it is clear that photoexcitation leads to PL; however, the quantum yield of this process at room temperature is low (~0.07),²⁷ suggesting that most of the radiation absorbed by the SiN_x is dissipated in the form of heat. Therefore, we claim that despite the weak absorption of 532 nm radiation by water, the heated SiN_x instantly heats the nearby electrolyte, rapidly forming a steady-state thermal gradient that is localized near the membrane.

To further look into this possibility, we have performed a finite-element continuum approach simulation (COMSOL Multiphysics). Figure 1d displays a heat map of the temperature surrounding a 43-nm-thick SiN_x membrane with a 12.5 mW beam focused at the pore. For this simulation, we have matched the materials properties and laser conditions to our experimental setup conditions (for more details see SI, Figure S2) and further assumed that all radiation absorbed by the SiN_x, yet not resulting in PL, dissipates as heat. This efficient localized heating of the nanoscale membrane interface results in significant temperature gradients that extend to hundreds of nm away from the membrane. The peak temperature at the pore, T_p , for this simulation, corresponds to a thermal gradient of $\Delta T \sim 70$ °C.

Apart from heating, another possible mechanism that can lead to ion current enhancement upon laser irradiation of the pore must be ruled out: in a recent study using a similar SiN_x pore, current enhancement was suggested to be due to a rise in the pore's surface charge.²⁶ To investigate, we have designed a cell that allows pore surface charge to be measured during laser excitation. The cell allows a pressure gradient (ΔP) to be applied to the *cis* chamber, facilitating streaming potential (ζ) measurements.^{28,29} In Figure 2a we show exemplary traces of ζ as a function of ΔP for different values of laser power (P) at the

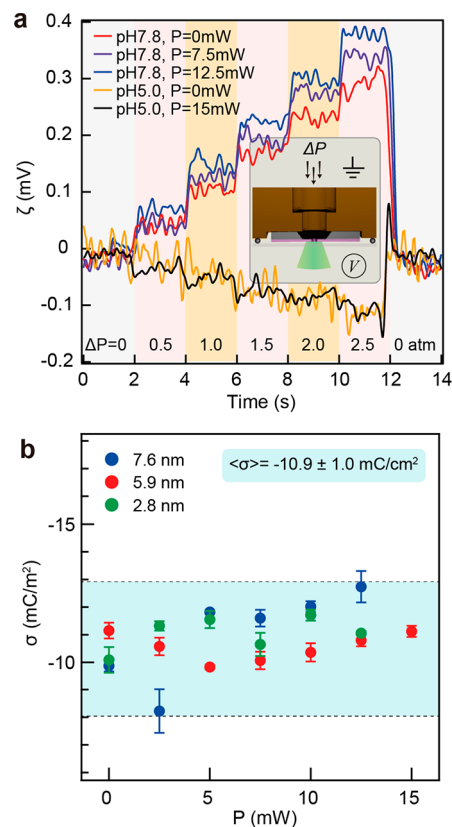


Figure 2. Pore surface charge measurements. (a) Streaming potential measurements carried out by applying 2 s pressure steps to the *cis* chamber of a nanopore and recording the streaming potential, ζ (electrolyte: 0.4 M KCl, pH 7.8 or pH 5.0). Data shown for several different laser powers, P , and pore sizes for pH 7.8 and pH 5.0 experiments are 7.6 and 5.5 nm, respectively. (b) Surface charge density σ vs laser power for three pores of diameters 7.6 (blue), 5.9 (red), and 2.8 nm (green) at pH 7.8. Shaded blue region represents the overall range of σ values measured (mean and st. dev. indicated in the figure).

pore. We have carried out these measurements at pH 7.8, the normal buffer conditions used in all experiments in this work, as well as pH 5.0, a more acidic condition that leads to SiN_x surface charge inversion.²⁸ Increasing ΔP leads to increasingly more positive ζ values at pH 7.8, since a positive bias at the *trans* chamber is required to neutralize the pressure-driven counterion streaming current (K⁺ ions). At pH 5.0, however, the opposite trend is seen, confirming surface charge inversion. More importantly, we find that ζ vs ΔP is relatively independent of P , that is, light does not appreciably impact the pore's surface charge. In Figure 2b we plot the pore surface charge density (σ) as a function of P for three different SiN_x pores at pH 7.8 with indicated diameters (see ref 29 for details). For all experiments and all laser powers at pH 7.8, we find that $\langle \sigma \rangle = -10.9 \pm 1.0$ mC/cm², whereas for the pH 5.0 experiment we find that $\sigma = +2.2 \pm 0.3$ mC/cm² for $P = 0$ mW and $\sigma = +2.7 \pm 0.2$ mC/cm² for $P = 15$ mW. For the 7.6 nm pore σ changed by 30% upon maximum irradiation, which is expected to contribute to a less than 3% enhancement of the ion current.¹⁴ Given our observation of a ~100% ion current enhancement, our conclusion is that the overwhelming mechanism that governs laser-induced ion current enhancement is a photothermal heating effect.

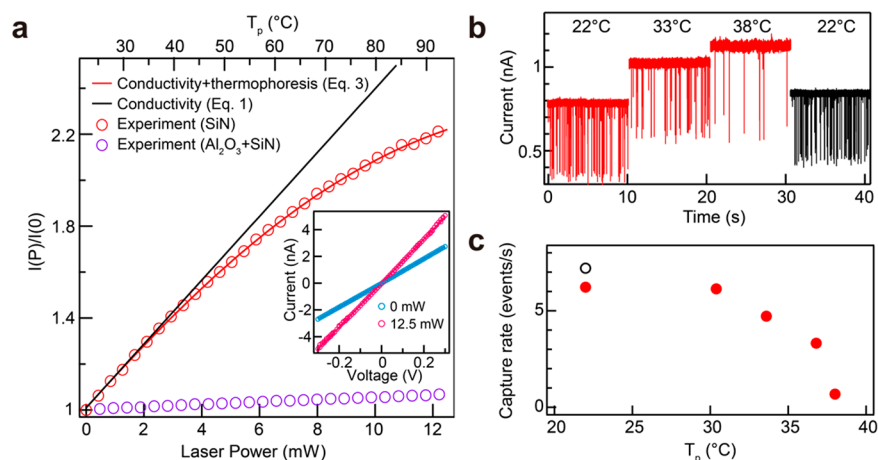


Figure 3. Pore thermometry from ion-current enhancement data. (a) Red circles: Measured current enhancement factors, $I(P)/I(0)$, as a function of laser power applied to a 3 nm diameter SiN pore with a 14.1 nm effective thickness ($V = 100$ mV). Purple circles: a 28 nm diameter pore with 16.5 nm thick Al_2O_3 and 5 nm thick SiN ($V = 100$ mV). The black curve represents a fit to a standard conductivity vs temperature model (see eq 1), whereas the red curve accounts for thermophoresis (see eq 3 and text for details). Inset shows I – V curves for the pore at $P = 0$ and 12.5 mW. The top scale is the corrected temperature obtained from the fits (note: this scale is not applicable to the $\text{Al}_2\text{O}_3 + \text{SiN}$ pore due to reduced heating by the laser). (b) Red traces: Continuous 10 s current trace samples for a 4 nm diameter pore with a 9.7 nm effective thickness when 30 nM 1 kbp double-stranded DNA is in the cis chamber, and 200 mV is applied to the trans chamber, at different indicated pore temperatures (T_p) induced by laser heating. The black trace was obtained using $P = 0$ mW after collecting data at increasing laser powers (note: slight pore expansion leads to higher baseline current, see Figure S9 for demonstration). (c) Red circles, black circle: Mean capture rates as a function of pore temperature for the experiments in panel b.

The direct measurement of temperature at a nanopore is extremely challenging. However, the relationship between pore conductance and electrolyte temperature has been previously studied in detail.²³ As the solution temperature increases, its viscosity decreases, resulting in increased ion mobilities and increased pore conductance. In Figure 3a, we present the fractional current enhancement, $I(P)/I(0)$, as a function of laser power for a 3 nm diameter pore under 100 mV applied voltage. In bulk, the solution conductivity has been determined to increase linearly with temperature in the range 0–100 °C, and the ion current can be expressed as a function of temperature using the following approximation,

$$I(T) = A\sigma(T) = A(a + bT) \quad (1)$$

where A is constant that depends on pore geometry and a and b are constants that depend on the electrolyte.²³ The black line in Figure 3a represents the expected enhancement as a function of temperature for this pore, where the coefficients a and b are 2.4 and 0.125, respectively.³⁰ Clearly, our experimental data deviates from the straight line defined by eq 1, as previously observed.²⁶

To explain our result, we refine eq 1 by considering the effect of thermophoresis, which describes the diffusion of species in a thermal gradient. Thermophoresis is a long-known effect in which species migrate in a thermal gradient due to the Soret effect. A species with a positive Soret coefficient (S_T) will diffuse toward a colder region, whereas a species with a negative value of S_T will diffuse toward the hotter region.³¹ Since our laser-induced heating causes a strong thermal gradient (see Figure 1d), the equilibrium ion concentration (C) at the pore should be affected by thermophoresis, an additive effect to thermal effects on solution conductivity. Thermodiffusion and the Soret coefficient are depicted as eqs 2 and 3, respectively:

$$C/C_0 = \exp[-S_T(T - T_{\text{room}})] \quad (2)$$

$$S_T = S_T^\infty \left[1 - \exp\left[\frac{T^* - T}{T_0}\right] \right] \quad (3)$$

where C_0 , S_T , T_{room} , S_T^∞ , T^* , and T_0 are the bulk species concentration, Soret coefficient, room temperature, a high- T thermophobic limit, the temperature where S_T switches sign, and the strength of temperature effects, respectively.^{31,32} Combining eqs 1, 2, and 3, we derive an expression for the ionic current enhancement, defined as the current as a function of power $I(P)$ normalized to the current without any laser applied $I(0)$, as a function of local pore temperature (for the complete equation, see SI):

$$I(P)/I(0) = I(T)/I(T_{\text{room}}) = C/C_0 \left[\frac{a + b(\Delta T + T_{\text{room}})}{a + bT_{\text{room}}} \right] \quad (4)$$

Our experimental data fit the model of eq 4 remarkably well, using the literature value of $S_T^\infty = 0.0098 \text{ K}^{-1}$,³³ and using fitting parameters for T_0 and T^* for KCl we obtain values of $T_0 = 193 \pm 5.0 \text{ K}$ and $T^* = 297 \pm 1.3 \text{ K}$ at room temperature ($T_{\text{room}} = 295 \text{ K}$). While our value for T_0 is higher than literature values, T^* is in good agreement with previous work.³³ After fitting the data, the emerging relationship between $I(P)/I(0)$ and the peak pore temperature (T_p) allows us to determine the pore temperature based on the current enhancement factor. The positive value of S_T for KCl dictates a reduction in the relative ion concentration (C/C_0) at the pore as laser power increases (for more details see SI, Figure S3). As comparison, a 28 nm pore with 16.5 nm thick Al_2O_3 and 5 nm thick SiN membrane shows considerably low $I(P)/I(0)$ as a function of laser power, which is attributed that charged carriers in SiNx induce heating. Also, laser power does not always produce the same enhancement from pore to pore, due to several factors that include variability in chemical composition of the pore, the exact focus position, and pore geometry.

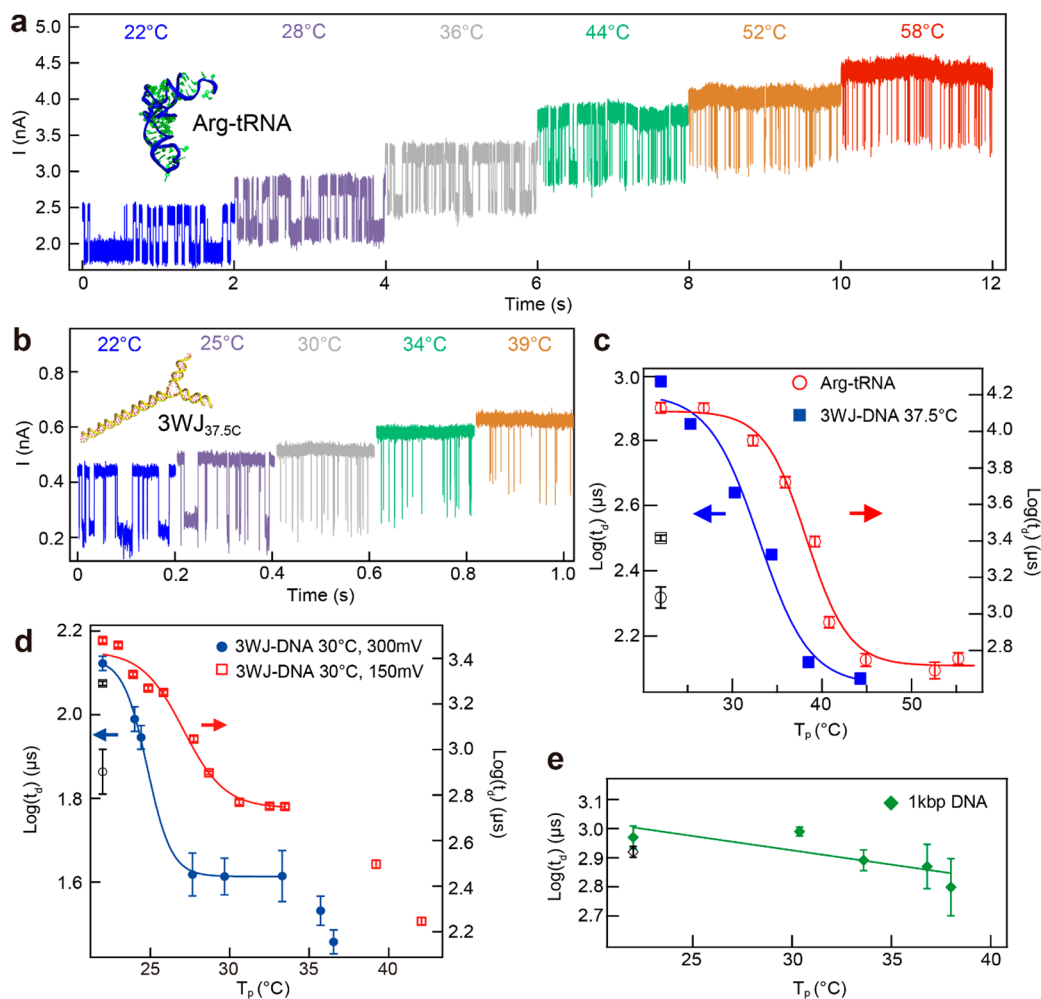


Figure 4. Single-molecule thermal melting. (a) Continuous 2 s current trace samples of Arg-tRNA at different T_p values (indicated above each respective trace) through a 3 nm diameter, 19.6 nm effective thickness pore ($V = 600$ mV). (b) Similar traces shown for three-way DNA junction $3WJ_{37.5}$ translocation through a 3 nm diameter pore with a 14.7 nm effective thickness at $V = 200$ mV for different T_p values. (c) Mean $\log(t_d)$ vs T_p for $3WJ_{37.5}$ and Arg-tRNA, as well as a sigmoid fit through each data set. Based on fit, T_m^* values of 33.0 and 38.3 °C were obtained for $3WJ_{37.5}$ and Arg-tRNA, respectively. (d) Mean $\log(t_d)$ vs T_p for $3WJ_{30C}$ under applied voltages of 150 mV and 300 mV using a 3 nm diameter pore with a 11.6 nm effective thickness, showing T_m^* values of 27.0 and 24.7 °C, respectively. (e) Control experiment of 1 kbp dsDNA translocations as a function of T_p using $V = 200$ mV. Black markers in panels c–e represent obtained data following the experiments, which show some hysteresis due to a slight pore expansion.

Further evidence for thermophoresis is seen by DNA capture behavior as a function of laser power. In Figure 3b, we show sample current traces obtained for a 30 nM sample of 1 kbp dsDNA added to the cis chamber of a 4 nm diameter pore ($V = 200$ mV) at different laser powers P . As P increases, we observe a monotonic reduction in DNA capture rates, which is restored when the laser is switched off to the original capture values (black trace). This suggests a positive value of S_T for DNA in KCl electrolyte, in accordance with a previous study using plasmonic heated pores.²⁴ A summary of DNA capture rates vs peak pore temperatures (T_p) is shown in Figure 3c. Our combined observations of DNA capture behavior and ion current enhancement emphasize the role of thermophoresis.

Using the current enhancement as a pore thermometer, we have investigated the role of temperature on nucleic acid secondary structure. In Figure 4a, we show 2 s long continuous current traces that depict the passage of Arg-tRNA molecules through a 3 nm pore at different temperatures in the range of 22–58 °C ($V = 600$ mV). The pore geometry requires tRNA deformation before its passage through the nanopore, while we

rationalize that the melted tRNA behaves much flexible and can smoothly pass through a pore.^{9,34} Dwell time (t_d) statistics should therefore allow us to distinguish molecular deformation below and above the thermal melting transition. The traces in Figure 4a show long dwell times for the Arg-tRNA near room temperature ($\langle t_d \rangle$ values of >10 ms), whereas increasing the pore temperature T_p results in markedly reduced $\langle t_d \rangle$ values, which we attribute to melting (see SI Figure S4 for scatter plots). To further confirm our hypothesis, we have carried out similar experiment in Figure 4b on a synthetic three-way junction (3WJ) DNA molecule, assembled from three DNA strands in a way that contains a branching site that melts at 37.5 °C under our experimental buffer conditions. We refer to this construct as $3WJ_{37.5C}$ (see SI Figure S5). As observed with Arg-tRNA, the transition in $\langle t_d \rangle$ vs T_p is evident from the pulse shapes for $3WJ_{37.5C}$ (see SI Figure S6 for scatter plots). A summary of $\langle t_d \rangle$ vs T_p for the two molecules, shown in Figure 4c, reveals sharp transitions at $T_m^* = 38.3 \pm 0.5$ °C and 33.0 ± 1.0 °C for Arg-tRNA and $3WJ_{37.5C}$, respectively. Similarly pronounced transitions toward faster $\langle t_d \rangle$ values were obtained

in other experiments with a different pore ($N = 2$ for tRNA and $N = 2$ for 3WJ). To further confirm that our measurements probe a thermal melting transition, we have designed and tested another 3WJ DNA molecule for which the melting temperature of a branching site is 30 °C, 3WJ_{30C}. In Figure 4d, we show $\langle t_d \rangle$ values vs T_p for two different applied voltages. The transitions we find ($T_m^* \sim 24$ and 27 °C) are lower than for 3WJ_{37.5C}, consistent with the expected melting temperature trend. Further, considering that voltage is a force perturbation of the molecule that should reduce the melting temperature T_m^* , it would make sense that increasing the voltage reduces the melting temperature transition point. Finally, as a negative control experiment against the data in Figure 4d, we tested the dwell times of a linear 1 kbp double-stranded DNA fragment in the range 22–38 °C, which reveals only a mild reduction in dwell times without any observed transition (see Figure 4e).

Force-induced impact on molecular melting transitions have been observed in AFM³⁵ and optical tweezers³⁶ measurements. For DNA melting, a finite change in heat capacity, ΔC_p , between the native and melted state is found,³⁷ which, after correction, yields a predictable relationship between melting temperature and the applied force on the molecule.³⁶ In the case where $\Delta C_p \sim 0$, a linear relationship between applied force and melting temperature is expected, which allows extrapolation of thermal melting vs force to obtain the zero-force melting temperature of the molecule. To test this, melting transition data for the molecule is needed at different forces, which, based on the approach in Figure 4, would require dwell-time data for several voltages at each temperature, totaling in ~ 30 –40 data sets. This limitation is overcome by developing a thermoscopic method for probing thermal melting in a single-molecule: In this alternative approach, we rapidly heat the molecule only after its capture in the pore and thereafter probe its melting dynamics. To design this experiment, we have borrowed from an analogous scheme of nanopore force spectroscopy in which detection of molecular capture in the pore triggers an immediate voltage ramp.^{38–41} In our case, however, molecular capture in the pore sends a voltage waveform to the electro-optic modulator within $\sim 4 \mu\text{s}$, which results in a prescribed laser power schedule that heats the individual molecule that is probed at the pore. Figure 5a shows a representative set of traces obtained using this method for Arg-tRNA. Normalized current traces are overlaid such that capture occurs at $t = 0$ ms, also the point at which the laser is swept to allow single-molecule heating. Interestingly, we observe fluctuating current signals in region “2”, possibly reflecting the molecule’s dynamics in the pore as a function of temperature prior to melting, whereas melting occurs when the current is restored to its increasing baseline value, clearly seen at point “3” for the highlighted trace. Pore thermometry is achieved from the open-pore ion current (see SI Figure S7 for details). For comparison, in the figure we show representative events (near the mean dwell times) for Arg-tRNA in which no ramp was applied, resulting in dwell times that typically exceeded the thermoscopy probing time (see SI Figure S8 for dwell time histograms). Getting back to melting temperatures, histograms of melting times/temperatures obtained for four different voltages are shown in Figure 5b. From the mean values of these histograms we obtain a plot of the average tRNA melting temperature as a function of applied voltage in Figure 5c. Using the fact that literature values of ΔC_p for Phe-tRNA are negligible under similar ionic strengths ($\Delta C_p \sim 0$ at 150 mM NaCl),⁴² we assume linearity between the applied force

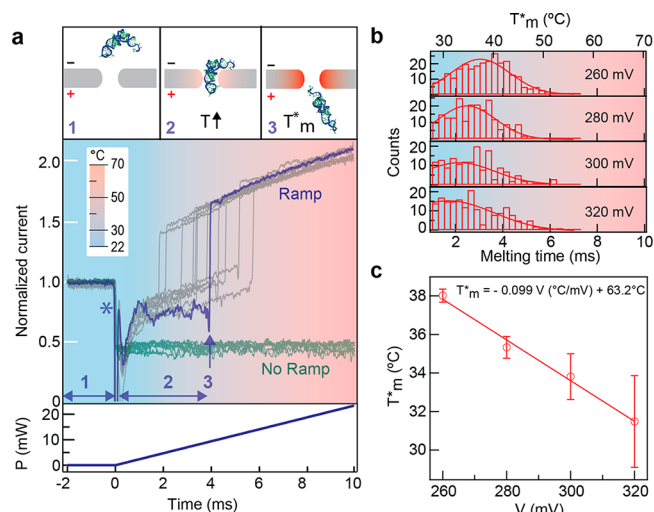


Figure 5. Thermoscopy for single-molecule melting determination. (a) Top: Schematic depiction of the three steps of single-molecule thermoscopy: 1. Constant voltage applied to capture an Arg-tRNA molecule, 2. Capture triggers thermal scan, achieved by a linear sweep of the laser power, P , 3. Molecular translocation through the pore at a melted state. Middle: Exemplary single-molecule normalized current traces obtained in Arg-tRNA thermoscopy for a 3 nm diameter pore with a 10.3 nm effective thickness, either without (green traces, $V = 350$ mV) and with (gray traces, $V = 300$ mV) thermal ramping. Capture of molecules is set to $t = 0$ ms. Bottom: Corresponding laser ramp (2.4 mW/ms). (b) Histograms of Arg-tRNA melting times obtained for different applied voltages, and corresponding melting temperatures shown on top axis. (c) Mean melting temperatures, T_m^* , as a function of voltage. The linear fit reveals a zero-force melting point of $T_m = 63.2$ °C, in agreement with tRNA bulk melting data from the literature (see text).

and melting transition temperature.³⁶ The resulting linear fit to the data yields an ordinate intercept of 63.2 °C, in very close agreement to tRNA melting temperature of 62 °C in 0.5 M NaCl.⁴³ We note that our information-rich approach of thermoscopy required four data sets at different voltages to achieve equilibrium melting point determination, in contrast to the many data sets required in the previous approach of point-by-point static temperature experiments shown in Figure 4. Finally, for the 3WJ_{30C} data in Figure 4d that contains two voltage points, if we neglect ΔC_p for the molecule we arrive at a crude melting temperature estimate of 30 °C, in excellent agreement to the bulk measurements.

We have demonstrated here a photothermal effect in which a visible laser irradiant on a silicon nitride nanopore causes nonradiative heating. This results in a highly localized thermal gradient around the pore that, depending on the laser power applied, can heat the surrounding environment to near boiling. The ion-current enhancement profile, in addition to DNA capture that decreases with increasing thermal gradient, are both consistent with thermophoretic effects. After correction for these effects, the ion-current enhancement provides a good measure of the pore temperature. Using temperature information, we have demonstrated single-molecule melting of three biomolecules, two control DNA molecules and one tRNA molecule. We observe a sharp transition in dwell times as a function of temperature that varies with the type of molecule tested, although all transition temperatures are lower than the bulk melting temperatures due to the applied force by the pore. This is resolved in thermoscopy experiments, in which

temperature is ramped for each molecule after its capture. A voltage dependence study reveals that the intercept of the melting temperature at zero voltage, hence zero force, corresponds well to the bulk melting temperature of a tRNA molecule. With these findings, further applications of localized heating/force measurements are enabled for future studies.

Nanopore Fabrication and Nanopore-Based Measurements. Nanopores were fabricated through freestanding, ~50-nm-thick, 20–50 μm in length SiN_x membranes which are supported by a $5 \times 5 \text{ mm}^2$ Si chip. The 50-nm-thick SiN_x layer was deposited using low-pressure chemical vapor deposition on 500- μm -thick $\langle 100 \rangle$ oriented Si wafer that has been prior to deposition thermally oxidized to provide a 2.5- μm -thick SiO_2 barrier layer to reduce electrical capacitance noise. Thin regions as optical markers were patterned as previously described³⁴ using lithography on the membrane side followed by reactive ion etching (RIE). For complete fabrication details see ref 44. To fabricate freestanding Al_2O_3 with SiN membrane, 150 cycles of atomic layer deposition (ALD) was employed to deposit 16.5 nm Al_2O_3 on membrane side. After Al_2O_3 deposition, 25 nm thick SiN was etched by 32 s RIE. The deposition rate of Al_2O_3 on SiN and the etching rate is 0.11 nm/cycle and 0.75 nm/s.

Transmission electron microscopy (JEOL 2010F) was then used to drill 2–8 nm pore through the SiN_x membrane. Prior to an experiment, nanopores were cleaned using freshly heated piranha solution (1:2 mixture of H_2O_2 and H_2SO_4) for 10–15 min. Nanopore chips were then assembled in a custom PTFE cell, and an Ag/AgCl electrode was inserted into each chamber. Unless otherwise stated, the electrolyte used for experiments in this paper contained 0.4 M KCl, 10 mM Tris, and 1 mM EDTA, buffered to pH 7.9. All pore diameters and effective thickness for measuring melting temperature in the paper were estimated from open current and ion current blockade of dsDNA translocation.³⁴ The effective thickness was typically one-third of the total membrane thickness. Arg-tRNA from *S. cerevisiae* was generously obtained from Barry Cooperman, UPenn. The DNA sequences (listed in SI) used to assemble the three-way junctions were designed manually. The correct assemblies were initially confirmed with NUPACK.⁴⁵ All DNA oligos were purchased from IDT (idtdna.com) and were gel-purified (8 M urea, 15% acrylamide). DNA strands were eluted from gel pieces using $1 \times$ TBE buffer with 0.3 M NaCl. Following precipitation in 2.5 volumes of 100% ethanol, DNA in the buffer was washed in 90% ethanol, vacuum-dried, and resuspended in doubly deionized water. To assemble the three-way junctions (3WJ), three DNA strands were mixed one-pot in equimolar concentration (1 μM final) and heated to 95 $^\circ\text{C}$ for 2 min. After cooling them to room temperature, the constructed 3WJ-DNA buffers were adjusted to 0.4 M KCl. Concentrations of Arg-tRNA and 3WJ-DNA samples in experiments were 450 pg/ μL and 20 nM, respectively. The current was recorded using an Axopatch 200B amplifier, and data were digitized at 250 kHz after filtering the current samples using the built-in Bessel filter at either 100 kHz for all data and 10 kHz for data shown in Figure 5. Further low-pass filtering prior to analysis we performed in software at 10 kHz for Arg-tRNA and 3WJ-DNA (37.5 $^\circ\text{C}$) and 20 kHz for 3WJ-DNA (30 $^\circ\text{C}$). Current blockades and dwell times were extracted from the current traces using custom Python software, developed in the Wanunu Lab (<https://github.com/rhenley/Pyth-Ion/>). In Figures 4 and 5, the temperature is calculated using $I(P)/I(0)$ as shown in Figure 3a. A detailed

calculation for the melting data analysis in Figure 5 is described in SI.

Finite-Element Simulations. We used COMSOL Multiphysics software to analyze theoretically the laser-induced temperature increase and the impact of electrical force on melting temperature. Briefly, for temperature calculations, we modeled a 42.5-nm-thick SiN_x membrane with a 3 nm diameter hourglass-shaped pore surrounded by electrolyte solution. Heat flux that corresponds to the laser power, after correcting for light reflection at all interfaces and photoluminescence emission, was applied from the bottom surface of membrane. The detailed approach, as well as the simulation model, are described in the SI.

■ ASSOCIATED CONTENT

Supporting Information

The Supporting Information is available free of charge on the ACS Publications website at DOI: 10.1021/acs.nanolett.7b03752.

Schematic diagram of the nanopore device for thermoscopy; temperature profile of a laser-heated SiN_x membrane with a nanopore; salt concentration profile induced by ion thermophoresis; tRNA translocation with laser heating; structure, melting profiles, and sequences of 3WJ-DNA; 3WJ-DNA translocations with laser heating; current trace during single-molecule thermoscopy and temperature calculation; Arg-tRNA translocation time before and after single-molecule thermoscopy (PDF)

■ AUTHOR INFORMATION

Corresponding Author

*E-mail: wanunu@neu.edu. Phone: +1-617-373-7412.

ORCID

Qing Zhao: 0000-0003-3374-6901

Meni Wanunu: 0000-0002-9837-0004

Notes

The authors declare no competing financial interest.

■ ACKNOWLEDGMENTS

This work was supported by funding from the National Science Foundation (EFMA-1542707, M.W.). H.Y. is a recipient of JSPS Postdoctoral Fellowships for Research Abroad. We would like to thank Jason Sutin for helpful advice, Barry Cooperman for tRNA donation, Mohammad Amin Alibakhshi for assistance with wafer processing, as well as Prof. Sotaro Uemura, Prof. Wataru Iwasaki, Prof. Toshiharu Saiki, and Prof. Mark C. Williams for valuable comments.

■ REFERENCES

- (1) Dekker, C. *Nat. Nanotechnol.* **2007**, *2*, 209–215.
- (2) Venkatesan, B. M.; Bashir, R. *Nat. Nanotechnol.* **2011**, *6*, 615–624.
- (3) Wanunu, M. *Phys. Life Rev.* **2012**, *9*, 125–158.
- (4) Shi, W.; Friedman, A. K.; Baker, L. A. *Anal. Chem.* **2017**, *89*, 157–188.
- (5) Kasianowicz, J. J.; Bezrukov, S. M. *Biophys. J.* **1995**, *69*, 94–105.
- (6) DeBlois, R. W.; Bean, C. P. *Rev. Sci. Instrum.* **1970**, *41*, 909–916.
- (7) Sauer-Budge, A. F.; Nyamwanda, J. A.; Lubensky, D. K.; Branton, D. *Phys. Rev. Lett.* **2003**, *90*, 238101.
- (8) Shasha, C.; Henley, R. Y.; Stoloff, D. H.; Rynearson, K. D.; Hermann, T.; Wanunu, M. *ACS Nano* **2014**, *8*, 6425–6430.

- (9) Henley, R. Y.; Ashcroft, B. A.; Farrell, I.; Cooperman, B. S.; Lindsay, S. M.; Wanunu, M. *Nano Lett.* **2016**, *16*, 138–144.
- (10) Manrao, E. A.; Derrington, I. M.; Laszlo, A. H.; Langford, K. W.; Hopper, M. K.; Gillgren, N.; Pavlenok, M.; Niederweis, M.; Gundlach, J. H. *Nat. Biotechnol.* **2012**, *30*, 349–353.
- (11) Garalde, D. R.; Snell, E. A.; Jachimowicz, D.; Heron, A. J.; Bruce, M.; Lloyd, J.; Warland, A.; Pantic, N.; Admassu, T.; Ciccone, J.; Serra, S.; Keenan, J.; Martin, S.; McNeill, L.; Wallace, J.; Jayasinghe, L.; Wright, C.; Blasco, J.; Sipos, B.; Young, S.; Juul, S.; Clarke, J.; Turner, D. *J. bioRxiv*, **2016**.
- (12) Henrickson, S. E.; Misakian, M.; Robertson, B.; Kasianowicz, J. *J. Phys. Rev. Lett.* **2000**, *85*, 3057–3060.
- (13) Meller, A.; Nivon, L.; Branton, D. *Phys. Rev. Lett.* **2001**, *86*, 3435–3438.
- (14) Smeets, R. M. M.; Keyser, U. F.; Krapf, D.; Wu, M.-Y.; Dekker, N. H.; Dekker, C. *Nano Lett.* **2006**, *6*, 89–95.
- (15) Lu, B.; Hoogerheide, D. P.; Zhao, Q.; Zhang, H.; Tang, Z.; Yu, D.; Golovchenko, J. A. *Nano Lett.* **2013**, *13*, 3048–3052.
- (16) Wanunu, M.; Sutin, J.; McNally, B.; Chow, A.; Meller, A. *Biophys. J.* **2008**, *95*, 4716–4725.
- (17) Holmstrom, E. D.; Dupuis, N. F.; Nesbitt, D. J. *Biophys. J.* **2014**, *106*, 220–231.
- (18) Hirsch, L. R.; Stafford, R. J.; Bankson, J. A.; Sershen, S. R.; Rivera, B.; Price, R. E.; Hazle, J. D.; Halas, N. J.; West, J. L. *Proc. Natl. Acad. Sci. U. S. A.* **2003**, *100*, 13549–13554.
- (19) Reiner, J. E.; Robertson, J. W. F.; Burden, D. L.; Burden, L. K.; Balijepalli, A.; Kasianowicz, J. J. *J. Am. Chem. Soc.* **2013**, *135*, 3087–3094.
- (20) Angevine, C. E.; Seashols-Williams, S. J.; Reiner, J. E. *Anal. Chem.* **2016**, *88*, 2645–2651.
- (21) Keyser, U. F.; Krapf, D.; Koeleman, B. N.; Smeets, R. M. M.; Dekker, N. H.; Dekker, C. *Nano Lett.* **2005**, *5*, 2253–2256.
- (22) Smeets, R. M. M.; Keyser, U. F.; Wu, M. Y.; Dekker, N. H.; Dekker, C. *Phys. Rev. Lett.* **2006**, *97*, 088101.
- (23) Jonsson, M. P.; Dekker, C. *Nano Lett.* **2013**, *13*, 1029–1033.
- (24) Nicoli, F.; Verschuere, D.; Klein, M.; Dekker, C.; Jonsson, M. P. *Nano Lett.* **2014**, *14*, 6917–6925.
- (25) Li, Y.; Nicoli, F.; Chen, C.; Lagae, L.; Groeseneken, G.; Stakenborg, T.; Zandbergen, H. W.; Dekker, C.; Van Dorpe, P.; Jonsson, M. P. *Nano Lett.* **2015**, *15*, 776–782.
- (26) Di Fiori, N.; Squires, A.; Bar, D.; Gilboa, T.; Moustakas, T. D.; Meller, A. *Nat. Nanotechnol.* **2013**, *8*, 946–951.
- (27) Giorgis, F.; Vinegoni, C.; Pavesi, L. *Phys. Rev. B: Condens. Matter Mater. Phys.* **2000**, *61*, 4693–4698.
- (28) Firnkes, M.; Pedone, D.; Knezevic, J.; Döblinger, M.; Rant, U. *Nano Lett.* **2010**, *10*, 2162–2167.
- (29) Waduge, P.; Hu, R.; Bandarkar, P.; Yamazaki, H.; Cressiot, B.; Zhao, Q.; Whitford, P. C.; Wanunu, M. *ACS Nano* **2017**, *11*, 5706.
- (30) Pezeshki, S.; Chimere, C.; Bessonov, A. N.; Winterhalter, M.; Kleinekathöfer, U. *Biophys. J.* **2009**, *97*, 1898–1906.
- (31) Dühr, S.; Braun, D. *Phys. Rev. Lett.* **2006**, *96*, 168301.
- (32) Iacopini, S.; Rusconi, R.; Piazza, R. *Eur. Phys. J. E: Soft Matter Biol. Phys.* **2006**, *19*, 59–67.
- (33) Römer, F.; Wang, Z.; Wiegand, S.; Bresme, F. *J. Phys. Chem. B* **2013**, *117*, 8209–8222.
- (34) Wanunu, M.; Dadosh, T.; Ray, V.; Jin, J.; McReynolds, L.; Drndic, M. *Nat. Nanotechnol.* **2010**, *5*, 807–814.
- (35) Clausen-Schaumann, H.; Rief, M.; Tolksdorf, C.; Gaub, H. E. *Biophys. J.* **2000**, *78*, 1997–2007.
- (36) Williams, M. C.; Wenner, J. R.; Rouzina, I.; Bloomfield, V. A. *Biophys. J.* **2001**, *80*, 1932–1939.
- (37) Chalikian, T. V.; Völker, J.; Plum, G. E.; Breslauer, K. J. *Proc. Natl. Acad. Sci. U. S. A.* **1999**, *96*, 7853–7858.
- (38) Bates, M.; Burns, M.; Meller, A. *Biophys. J.* **2003**, *84*, 2366–2372.
- (39) Mathé, J.; Arinstein, A.; Rabin, Y.; Meller, A. *Europhys. Lett.* **2006**, *73*, 128.
- (40) Tropini, C.; Marziali, A. *Biophys. J.* **2007**, *92*, 1632–1637.
- (41) Langecker, M.; Ivankin, A.; Carson, S.; Kinney, S. R. M.; Simmel, F. C.; Wanunu, M. *Nano Lett.* **2015**, *15*, 783–790.
- (42) Hinz, H.-J.; Filimonov, V. V.; Privalov, P. L. *Eur. J. Biochem.* **1977**, *72*, 79–86.
- (43) Riesner, D.; Maass, G.; Thiebe, R.; Philippsen, P.; Zachau, H. G. *Eur. J. Biochem.* **1973**, *36*, 76–88.
- (44) Carson, S.; Wilson, J.; Aksimentiev, A.; Wanunu, M. *Biophys. J.* **2014**, *107*, 2381–93.
- (45) Zadeh, J. N.; Steenberg, C. D.; Bois, J. S.; Wolfe, B. R.; Pierce, M. B.; Khan, A. R.; Dirks, R. M.; Pierce, N. A. *J. Comput. Chem.* **2011**, *32*, 170–173.